

Article

# Dynamic Doppler Characteristics of Maritime Airborne Corner Reflector

Lingang Wu , Shengliang Hu, Chengxu Feng \*, Yasong Luo, Zhong Liu and Li Lin

College of Weaponry Engineering, Naval University of Engineering, Wuhan 430033, China; oucwlq@163.com (L.W.)

\* Correspondence: kerryfengcx@126.com

**Abstract:** The maritime airborne corner reflector (ACR) is a radar reflector that can measure wind speed in an unknown sea area in real time over a long distance. To improve our understanding of how the ACR works, we investigated the Doppler characteristics of the ACR for the first time from a dynamic perspective. First, we constructed a radar echo signal model of the ACR. Then, we obtained the dynamic Doppler characteristics through pulse Doppler processing and discussed the special phenomenon of Doppler broadening. Finally, we proposed a rectangular window decomposition method to analyze the inner principle of the Doppler broadening phenomenon in more detail. In conclusion, this study provides valuable insights into the Doppler characterization of an ACR from a dynamic viewpoint, which contributes to enriching the basic theory of this equipment.

**Keywords:** airborne corner reflector; radar echo signal model; Doppler characteristics; Doppler broadening

## 1. Introduction

Corner reflectors, a type of radar-reflecting equipment [1,2], redirect incident rays back to their original direction through a three-sided metal corner structure, thereby generating a robust echo signal. Traditional maritime corner reflector devices are typically deployed using carrier fixation and inflatable floating methods. However, in recent years, airborne corner reflectors (ACRs) have emerged as a novel focus in the field of maritime corner reflection. ACRs are launched into the air using conventional carriers for efficient signal reflection. Notable versions of ACRs include [3] “WIZARD” developed by Rafael Corporation, “OCR” developed by Rheinmetall Corporation, “SEALEM” developed by Lacroix Defense Corporation, and “TORERO” jointly developed by IHI Aerospace Corporation and Chemring Group. These ACRs share similar design characteristics: supplementary parachutes serve as the primary solution for extending their operational duration; Octahedral Reflector (OR) structures constitute the mainstream approach for enhancing reflective capability. This paper primarily focuses on an ACR configuration featuring the typical modality of “parachute + OR”, as illustrated in Figure 1.

Due to the inherent disparity between ACRs and traditional corner reflectors in terms of modality, scholars have conducted a series of theoretical investigations into their jamming mechanism. Kubicke [4–6] proposed a hybrid algorithm based on Physical Optics (PO), Geometric Optics (GO), and the equivalent current method, which was employed to examine the polarization characteristics of OR structures. Zhang [7] introduced a high-frequency hybrid algorithm grounded in PO and area projection, enabling the establishment of a statistical model of a Radar Cross Section (RCS) [8] of the OR array. Luo [9] simulated the RCS of ORs with diverse geometric features using the Shooting and Bouncing Ray (SBR) method, summarizing regulars of its RCS concerning the angles and radius. However, these aforementioned studies primarily concentrate on electromagnetic scattering properties of OR structures under instantaneous static conditions.



**Citation:** Wu, L.; Hu, S.; Feng, C.; Luo, Y.; Liu, Z.; Lin, L. Dynamic Doppler Characteristics of Maritime Airborne Corner Reflector. *J. Mar. Sci. Eng.* **2024**, *12*, 727. <https://doi.org/10.3390/jmse12050727>

Academic Editor: Lev Shemer

Received: 24 March 2024

Revised: 21 April 2024

Accepted: 26 April 2024

Published: 27 April 2024



**Copyright:** © 2024 by the authors. Licensee MDPI, Basel, Switzerland. This article is an open access article distributed under the terms and conditions of the Creative Commons Attribution (CC BY) license (<https://creativecommons.org/licenses/by/4.0/>).

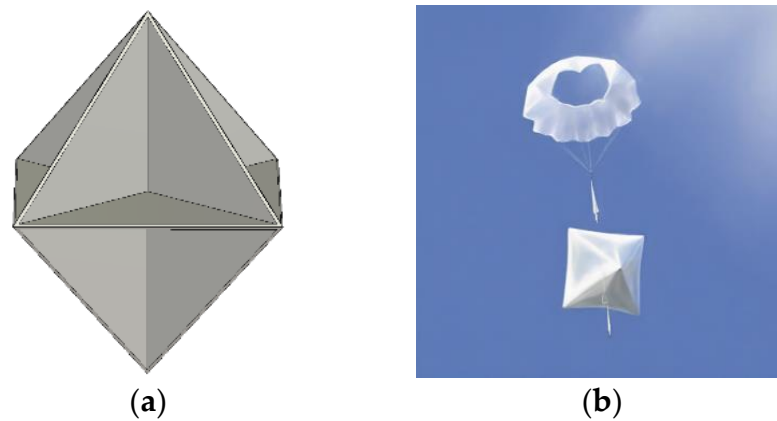


**Figure 1.** Typical modality of ACR. (a) Structure of Octahedral Reflector. (b) Parachute stagnation assist.

One particular application of maritime ACR equipment at sea involves the determination of long-distance sea-surface wind speed. In situations where obtaining accurate ambient wind speed in an unknown sea area is necessary, but telemetry is insufficient to meet accuracy requirements or when it is impractical to directly dispatch a carrier with an anemometer for data collection in close proximity, ACRs offer a unique advantage. By launching an ACR into the desired location at sea, it can steadily move along with the wind [10]. Then, the velocity of the floating ACR can be measured in real time using radar, based on the Doppler principle. Therefore, studying the Doppler characteristics of ACR targets holds significant practical importance.

The electromagnetic scattering characteristics of airborne motion radar targets, specifically ACRs, have only been analyzed under static conditions, which presents certain limitations and one-sidedness. The existing static target characterization of ACRs does not encompass or support the study of Doppler characteristics. To analyze the dynamic characteristics of ACR targets, a real-time Radar Cross Section (RCS) estimation method for OR structures [11] and a motion model [10] of maritime ACRs at sea were proposed in our previous work. These research works laid an important foundation for conducting dynamic Doppler characterization of ACRs. The innovation in this study primarily lies in the following aspects:

1. Constructing a radar echo signal model of the ACR target based on a pulsed linear frequency modulation (FM) signal;
2. Analyzing the dynamic Doppler characteristics of ACR targets using the pulse Doppler principle, and finding a special Doppler broadening phenomenon that hinders velocity measurement;
3. Analyzing the effects of different ACR conditioning parameters on the severity and frequency of Doppler broadening, and finding that the rotational rate of an ACR is the main factor affecting the broadening phenomenon;
4. A spectrum analysis method based on rectangular window decomposition was proposed to reveal the inherent causes of the Doppler broadening phenomenon and prove that Doppler broadening is indeed closely related to the rotational motion of ACRs.

Section 1 focuses on constructing the radar echo signal model of an ACR. Section 2 involves obtaining a time series Doppler characteristic image based on pulse Doppler processing and discussing the correlation between multiple condition parameters and Doppler broadening. Section 3 introduces an analytical method based on rectangular window decomposition and investigates the causes of Doppler broadening.

## 2. Radar Echo Signal Modeling for ACR

Modern radar technology pursues a greater signal bandwidth. Linear frequency modulation (LFM) signals [12], commonly used for matched-filter pulse compression, achieve a large time–broadband product by employing nonlinear phase modulation.

The LFM rectangular pulse signal is one of the most commonly used radar-transmitting signals. Its complex expression is

$$s_t(t) = \text{rect}\left(\frac{t}{T_p}\right) A_t \exp\left[j2\pi\left(f_c t + \frac{\mu}{2} t^2\right)\right] \tag{1}$$

where  $T_p$  is the pulse width,  $A_t$  is the transmit signal amplitude,  $f_c$  is the signal carrier frequency,  $\mu = B/\tau$  is the FM slope,  $B$  is the signal bandwidth, and  $\text{rect}(\cdot)$  is the rectangular function:

$$\text{rect}\left(\frac{t}{T_p}\right) = \begin{cases} 1 & \left(|t/T_p| \leq 1/2\right) \\ 0 & \left(|t/T_p| > 1/2\right) \end{cases} \tag{2}$$

When processing the echo signal from a target, we need to account for various factors like propagation loss, the target reflection coefficient, and the distance traveled. These factors influence both the amplitude and phase of the transmitted signal. The complex expression for the echo signal is

$$s_r(t) = \text{rect}\left(\frac{t - t_d}{T_p}\right) A_r \exp\left[j2\pi\left(f_c(t - t_d) + \frac{\mu}{2}(t - t_d)^2\right)\right] \tag{3}$$

where  $A_r$  is the echo signal amplitude and  $t_d$  is the echo time delay. The time delay ( $t_d$ ) of the echo in relation to the transmitted signal is directly proportional to the distance ( $d$ ) between the radar and the target:

$$t_d = \frac{2d}{c} \tag{4}$$

where  $c$  denotes the speed of light.

The center of mass of an ACR target serves as the scattering center [10]. The distance traveled by all the rays reflected by it equals twice the distance between the radar and the scattering center [13]. Consequently, the ACR can be regarded as a point-target scatterer. For simple point-target scatterers, the effect of the scattering process on the signal amplitude measured by the radar can be analyzed using the radar range equation.

The radar range equation provides a deterministic model that correlates the received echo power ( $P_r$ ) to the transmitted signal power ( $P_t$ ) through various parameters. In the case of high-carrier-frequency radars (X-band), assuming that the adopted LFM bandwidth is much smaller than the signal carrier frequency ( $B/f_c < 1/10$ ), the echo signal can still be considered a narrowband pulse. The received power ( $P_r$ ) estimated from the range equation can be directly related to the amplitude ( $A_r$ ) of the received pulse signal.

According to the radar range equation, the total backscattered power obtained by the receiving antenna is [14,15]

$$P_r = \frac{P_t G^2 \lambda^2 \sigma}{(4\pi)^3 d^4 L_s L_\alpha(d)} \tag{5}$$

where  $\lambda = c/f_c$  is the signal wavelength,  $\sigma$  is the RCS value that represents the ability of the target to reflect the radar wave,  $G$  is the antenna power gain,  $L_s$  is the system loss factor, and  $L_\alpha(d)$  is the atmospheric attenuation factor associated with distance,  $d$ .

Since the radar signal power is proportional to the square of the electric field strength, the amplitude of the target echo signal can be estimated using the following range equation:

$$\begin{aligned} A_r &= \sqrt{\frac{A_t^2 G^2 \lambda^2 \sigma}{(4\pi)^3 d^4 L_s L_\alpha(d)}} \\ &= \frac{|A_t| G \lambda}{8d^2} \sqrt{\frac{\sigma}{\pi^3 L_s L_\alpha(d)}} \end{aligned} \tag{6}$$

Substituting Equations (4) and (6) into Equation (3) yields an echo signal model of an ACR within a pulse repetition interval (PRI).

Therefore, the ACR echo signal is described as a complex model that incorporates multiple parameters. These parameters consist of radar system parameters influenced by

factors like the transmit signal amplitude, carrier frequency, bandwidth, and antenna gain. Additionally, there are unknown parameters related to the condition of the ACR target, such as the RCS and distance.

The acquisition of the RCS and distance necessitates additional ACR motion modeling. Reference [10] provides a comprehensive analysis and introduction of ACR motion characteristics, facilitating the establishment of a simplified ACR motion model. The typical motion process of the ACR consists of two distinct phases: “rapid descent” and “steady descent”. During the rapid descent phase, which lasts only for a few seconds, the ACR descends rapidly with vigorous oscillations and rotations. In this phase, its horizontal speed undergoes changes until it matches that of the wind speed. Subsequently, in the subsequent steady descent phase, the ACR gradually descends at a constant speed while maintaining horizontal rotational motion. At this stage, its horizontal velocity remains consistent with that of the wind speed. Due to the short duration of the rapid descent phase and the complexity of the motion process, a general ACR motion model is established primarily based on the steady descent phase:

$$\begin{cases} x = \sqrt{d_0^2 - z_0^2} \cos \phi_0 + v_x t \\ y = \sqrt{d_0^2 - z_0^2} \sin \phi_0 + v_y t \\ z = z_0 + v_z t \\ d = \sqrt{x^2 + y^2 + z^2} \\ \vartheta = \frac{\pi}{2} + \arcsin\left(\frac{z}{d}\right) \\ \phi = \phi_0 + \omega t \end{cases} \quad (7)$$

where  $(x, y, z)$  denotes the real-time position of the ACR;  $(v_x, v_y)$  denotes the wind speed in the horizontal direction;  $d_0$  denotes the initial distance between the radar and the ACR;  $\phi_0$  denotes the initial incidence azimuth;  $z_0$  denotes the initial altitude of the ACR;  $v_z$  denotes the vertical descent speed of the ACR, which is a fixed value related to the performance of the parachute and the overall mass of the system;  $d$  denotes the real-time distance between the radar and the ACR;  $\vartheta$  denotes the radar incidence pitch;  $\phi$  denotes the radar incidence azimuth; and  $\omega$  denotes the angular speed of the ACR’s horizontal rotational motion.

The real-time distance ( $d$ ) can be easily obtained from the ACR motion model. After obtaining the longitudinal and transverse angles ( $\vartheta$  and  $\phi$ ) of the radar incident wave, the RCS value of the ACR can be further obtained based on the geometrical optics method [16]:

$$\sigma = 4\pi \left( A_e^2 / \lambda^2 \right) \quad (8)$$

where  $A_e$  is the equivalent flat plate area, whose formula has different forms at different angles [11]:

- (1) When  $\vartheta$  approaches  $0^\circ$ , or  $\vartheta$  approaches  $90^\circ$  and  $\phi$  approaches  $0^\circ$  or  $90^\circ$ ,

$$A_e = 2 \exp\left(-\vartheta^2 / \zeta^2\right) \cdot L^2 \quad (9)$$

- (2) When  $\vartheta$  approaches  $90^\circ$ ,  $\phi$  approaches  $0^\circ$ , or  $\phi$  approaches  $90^\circ$ ,

$$\begin{cases} A_e = 2 \exp\left(-(\vartheta - 90)^2 / \zeta^2\right) \cdot L^2 \cdot \begin{cases} \sin \vartheta & 0 < \phi \leq 45^\circ \\ \cos \vartheta & 45^\circ < \phi < 90^\circ \end{cases} & \text{if } \vartheta \text{ close to } 90^\circ \\ A_e = 2 \exp\left(-\phi^2 / \zeta^2\right) \cdot L^2 \cdot \begin{cases} \sin \phi & 0 < \vartheta \leq 45^\circ \\ \cos \phi & 45^\circ < \vartheta < 90^\circ \end{cases} & \text{if } \phi \text{ close to } 0^\circ \\ A_e = 2 \exp\left(-(\phi - 90)^2 / \zeta^2\right) \cdot L^2 \cdot \begin{cases} \sin \phi & 0 < \vartheta \leq 45^\circ \\ \cos \phi & 45^\circ < \vartheta < 90^\circ \end{cases} & \text{if } \phi \text{ close to } 90^\circ \end{cases} \quad (10)$$

(3) When  $2^\circ < \vartheta < 88^\circ$  and  $2^\circ < \phi < 88^\circ$ ,

$$A_e = L^2 \cdot \begin{cases} 2 \sin^2 \vartheta \cdot \sin(2\phi + 90^\circ) / f(\vartheta, \phi) & \vartheta < \vartheta_1 \\ f(\vartheta, \phi) - 2 / f(\vartheta, \phi) & \vartheta_1 < \vartheta < \vartheta_2 \\ 2 \sin(\phi + 45^\circ) \cdot \sin(2\vartheta) / f(\vartheta, \phi) & \vartheta > \vartheta_2 \end{cases} \quad (11)$$

$$\vartheta_1 = \operatorname{arccot} \left[ \sqrt{2} \sin(\phi + 45^\circ) \right] \quad \vartheta_2 = \operatorname{arccot} \left[ \sqrt{2} \cos(\phi + 45^\circ) \right]$$

$$f(\vartheta, \phi) = \sin \vartheta \cdot [\cos \phi + \sin \phi] + \cos \vartheta$$

$L$  is the length of the inner edge of the ACR, typically representing its size;  $\zeta$  is the standard deviation of the normal distribution used to model the changing trend of  $A_e$  when the aspect angle is approaching the angular split.

### 3. Analysis of Dynamic Doppler Characteristics

The processing of echo signals by radar typically involves two steps, fast-time processing and slow-time processing [17], as illustrated in Figure 2. Fast-time processing, often referred to as pulse compression techniques, focuses on processing a single pulse echo to extract a range of information about the target. However, radars typically emit not just a single pulse but a periodic sequence of pulses. Typically, a coherent processing interval (CPI) of  $M$  pulses is utilized. Within each CPI, slow-time processing can gather velocity information about the target.

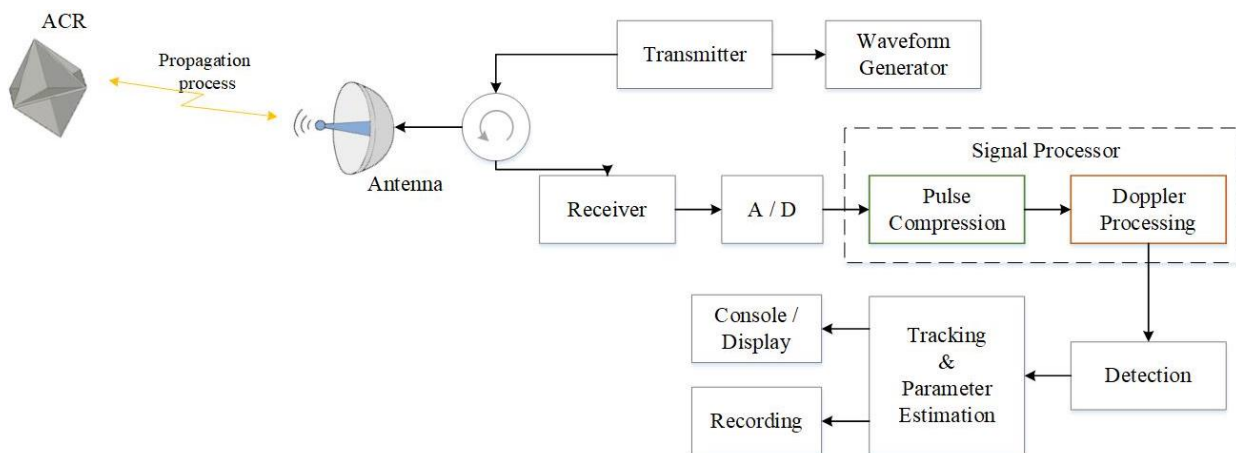


Figure 2. Pulsed Doppler radar workflow diagram.

The echo signal of multiple pulses can be expressed as follows [18]:

$$s_r(t, t_m) = \operatorname{rect} \left( \frac{t - t_m}{T_p} \right) A_r \exp \left[ j2\pi \left( f_c(t - t_m) + \frac{\mu}{2}(t - t_m)^2 \right) \right] \quad (12)$$

The above equation contains two independent variables, where  $t$  is the fast-time independent variable and  $t_m$  is the slow-time independent variable.  $t_m$  denotes the time delay of the  $m$ -th pulse echo, which is expressed as

$$t_m = \frac{2(d - v_d m T_r)}{c} \quad 1 \leq m \leq M \quad (13)$$

where  $T_r$  denotes the PRI; the radial velocity ( $v_d$ ) denotes the projection of the target velocity vector in the radar line-of-sight direction, which is positive when the target is moving in the direction of approaching the radar, and negative when it is moving in the opposite direction.

Pulse compression on each of the  $M$  signals yields  $M$  fast-time samples:

$$\chi(t, m) = A_r T_p \operatorname{sinc} \left[ B \left( t - \frac{2(d - v_d m T_r)}{c} \right) \right] \exp \left( -j2\pi f_c \frac{2(d - v_d m T_r)}{c} \right) \quad (14)$$

At this point, the slow-time independent variable is transitioned from the time delay ( $t_m$ ) to  $m$ , denoting the PRI sequence number. The fast-time independent variable ( $t$ ) is regarded as a constant during slow-time processing. By further isolating the terms independent of  $m$  to simplify the equation, the slow-time series with respect to  $m$  is obtained:

$$\chi[m] = A_r T_p \exp\left(-j2\pi f_c \frac{2d}{c}\right) \text{sinc}\left[B\left(t - \frac{2d}{c}\right) + m \frac{v_d T_r}{\Delta d}\right] \exp\left(j2\pi f_c \frac{2v_d}{c} m T_r\right) \quad (15)$$

where  $\Delta d = c/2B$  denotes the distance resolution.

The spectral form of the slow-time series  $\chi[m]$  is complex but can be analyzed using the Discrete Time Fourier Transform (DTFT) [19]. Let

$$A_r T_p \exp\left(-j2\pi f_c \frac{2d}{c}\right) \text{sinc}\left[B\left(t - \frac{2d}{c}\right) + m \frac{v_d T_r}{\Delta d}\right] \Leftrightarrow X(\omega) \quad (16)$$

be a DTFT pair.  $\omega$  denotes the normalized digital domain corner frequency. Despite the complex form of  $X(\omega)$ , there is no shifting of the spectrum. The DTFT of the slow-time series  $\chi[m]$  can be obtained from the frequency shift property as follows:

$$\chi[m] \Leftrightarrow Y(\omega) = X\left(\omega - 2\pi f_c \frac{2v_d}{c} T_r\right) \quad (17)$$

The spectral center of the slow-time series  $\chi[m]$  is shifted to  $\omega_0 = 2\pi f_c (2v_d/c) T_r$ . In addition, the velocity information of the target is included in the position of the spectral center of the slow-time series. Hence, the extraction of velocity information is accomplished by performing the slow-time Fast Fourier Transform (FFT) to identify the position of the spectral center. The relationship between the digital domain angular frequency ( $\omega$ ) and the true frequency ( $f$ ) is

$$\omega_0 = 2\pi f_c \frac{2v_d}{c} T_r = 2\pi \frac{f_d}{f_r} \quad (18)$$

The Doppler frequency shift equation can be derived from the following equation:

$$f_d = f_c \frac{2v_d}{c} \quad (19)$$

To further analyze the spectrum of the slow-time series  $\chi[m]$ , Equation (15) is simplified by considering the general case  $\Delta d \ll v_d T_r$ :

$$\begin{aligned} \chi[m] &= A_r T_p \exp\left(-j2\pi f_c \frac{2d}{c}\right) \text{sinc}\left(Bt - \frac{d}{\Delta d}\right) \exp(j2\pi f_d m T_r) \\ &= A \exp(j2\pi f_d m T_r) \\ &(m = 0, \dots, M - 1) \end{aligned} \quad (20)$$

The spectrum of  $\chi[m]$  is obtained by applying a DTFT to the above equation:

$$\begin{aligned} Y(f) &= \sum_{m=-\infty}^{+\infty} \chi[m] \exp(-j2\pi f m T_r) \\ &= A \frac{\sin[\pi(f-f_d)MT_r]}{\sin[\pi(f-f_d)T_r]} \exp[-j\pi(M-1)(f-f_d)T_r] \\ &\left(-\frac{PRF}{2} \leq f < \frac{PRF}{2}\right) \end{aligned} \quad (21)$$

$Y(f)$  is an asinc function with a peak at  $f = f_d$  and an amplitude peak at  $MA$ . The Doppler Equation (19) maps the frequency domain to the velocity domain and yields the radial velocity of the target by finding the location of the peak of the spectrum  $Y(f)$ .

The signal processing process described above is also known as pulsed Doppler processing [20–23]. In actual pulsed Doppler processing, the set of fast-time sample series with length  $N$  obtained from each  $M$  PRIs is typically regarded as a two-dimensional fast-time–slow-time data matrix  $\chi[n, m]$  within a CPI. Here, the dimension ( $n$ ) where the range

cells are located is termed the fast-time axis, while the dimension ( $m$ ) where the number of pulses is located is termed the slow-time axis. Pulse Doppler processing involves extracting the slow-time data series per range cell from the data matrix  $\chi[n,m]$  and conducting Discrete Fourier Transform (DFT) [24–27] on it. Ultimately, the fast-time–slow-time data matrix is transformed into a Range-Doppler (RD) data matrix  $Y[n,m]$ , as depicted in Figure 3.

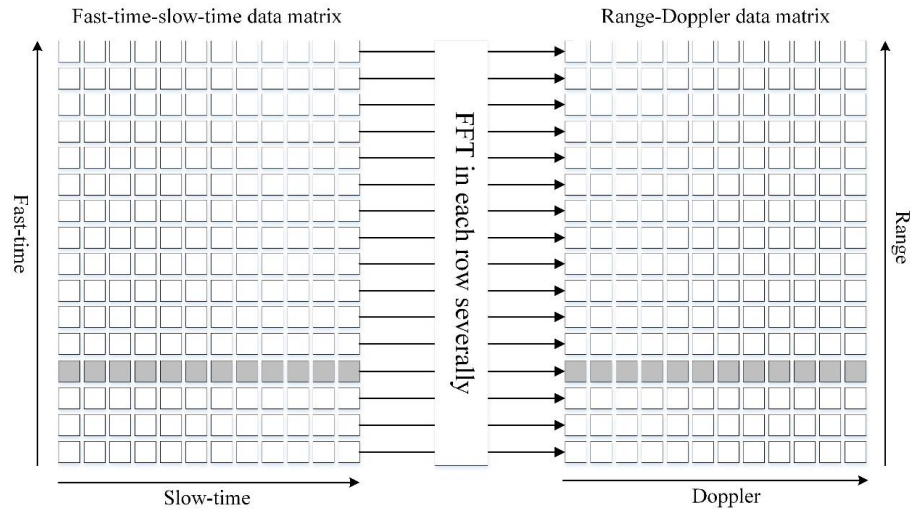


Figure 3. Processing of pulsed Doppler data.

The following parameters for radar operation are configured: carrier frequency:  $f_c = 10$  GHz, wavelength:  $\lambda = 0.03$  m, transmit power:  $P_t = 35$  kW, antenna gain:  $G = 60$ , bandwidth:  $B = 60$  MHz, pulse width:  $T_p = 2 \times 10^{-4}$  s, pulse repetition interval:  $T_r = 1 \times 10^{-3}$  s, coherent processing period:  $M = 64$ , and initial incident azimuthal angle:  $\phi_0 = 0^\circ$ . In the hypothetical case, an ACR target with a size  $L = 1$  m appears at the moment  $t = 0$  at a range  $d_0 = 1000$  m from the radar, with an initial height of 100 m in the air, a horizontal rotational rate of 0.5 rad/s, a dropping velocity of 1 m/s, and an ambient wind speed of (5, 0, 0) m/s. At this point, the fast-time–slow-time data matrix is obtained by pulse compression, i.e., the fast-time pulse compression output of all pulse signals within a CPI, as illustrated in Figure 4.

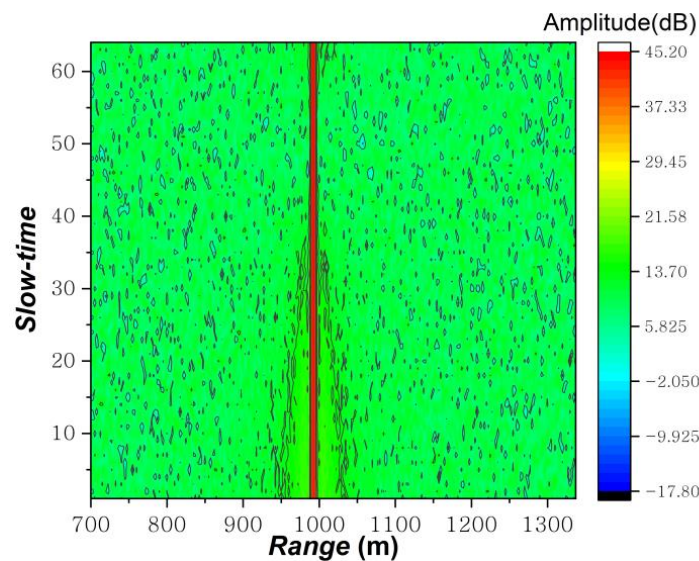


Figure 4. Fast-time–slow-time data graph.

In the above figure, the horizontal coordinate represents the fast-time (range) axis, while the vertical coordinate represents the slow-time (number of pulses) axis. DFT was separately performed on each row of the slow-time data series, resulting in the RD data plot as illustrated in Figure 5.

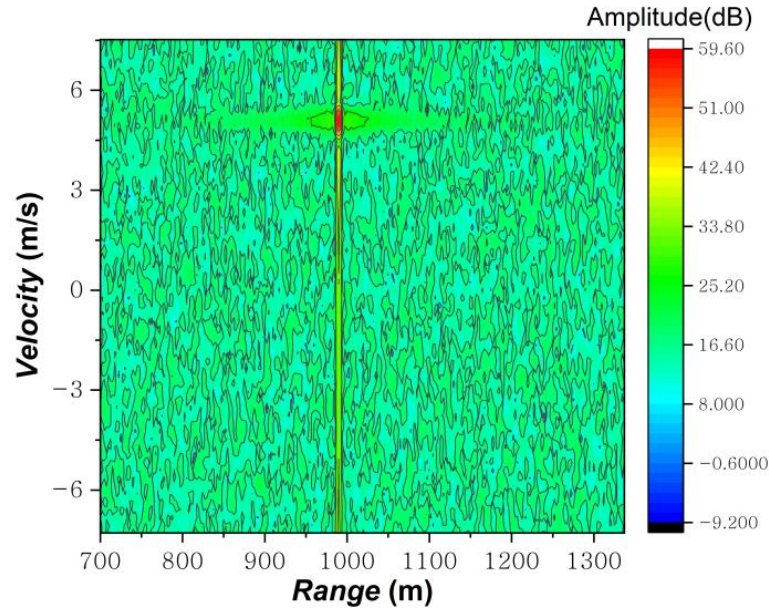


Figure 5. RD data graph.

The slow-time series within the range cell where the target is situated is compressed into a spike. Furthermore, the spike's location is consistently indicated to be at 5 m/s in the velocity dimension, aligning with the actual radial velocity magnitude. It indicates that the pulsed Doppler processing effectively extracted the velocity information of the target.

To analyze the dynamic Doppler characteristics of the ACR target over time, a single CPI was regarded as a frame, wherein each frame consisted of  $M$  PRIs. Pulse compression was subsequently performed on the echo signals within each PRI to obtain fast-time–slow-time data matrices. Following this, spectral analysis is performed on the slow-time series of the range cell where the target is located.

With  $T_0 = 0$  s as the initial moment and  $T_{end} = 2$  s as the final moment, a total of 31 frames were generated under the set PRI and CPI conditions. The generated dynamic sequential Doppler spectrogram is shown in Figure 6.

Over time, the peak of the Doppler spectrum consistently close to 5 m/s. This occurs because the flight direction of the ACR aligns with the radar's line-of-sight direction, and the flight speed of the ACR is very close to the wind speed (5 m/s). An interesting phenomenon arises when the Doppler spectrum of the ACR target exhibits significant broadening at specific moments, such as frames 4, 12, 20, and 28.

The presence of Doppler broadening is detrimental to detecting target velocity. When broadening occurs, the energy that was originally concentrated in the spectrum is dispersed, which perhaps causes false dismissal of an ACR target because the peak value of the spectrum may be lower than the detection threshold [28–30], as shown in Figure 7. Target false dismissal will destabilize target tracking and perplex later data analysis. Therefore, the Doppler broadening phenomenon should be minimized or avoided as far as possible.

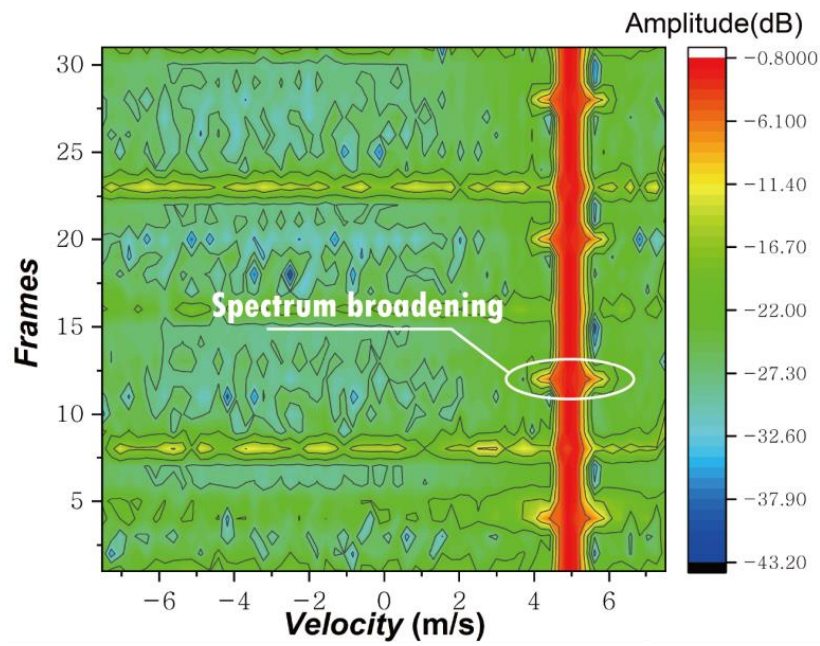


Figure 6. Sequential Doppler spectrogram.

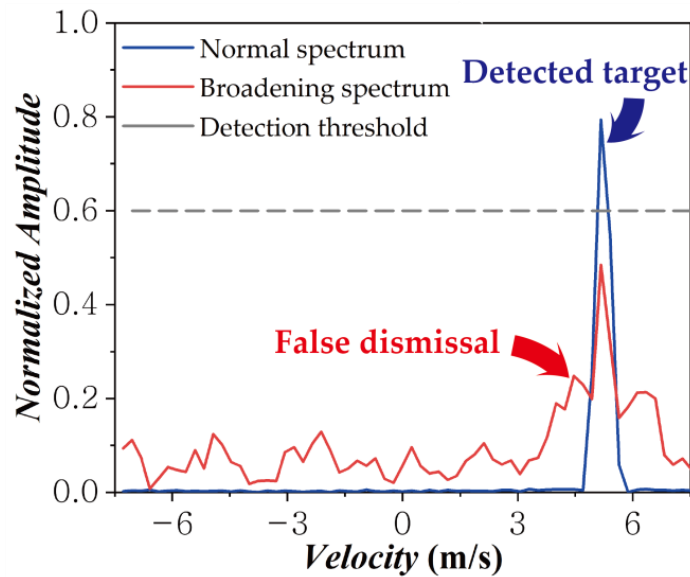


Figure 7. Target false dismissal caused by Doppler spectrum broadening.

In order to quantify the severity of Doppler broadening, the kurtosis [31–34] of the spectrum in the  $t$ -th frame is extracted:

$$K[t] = \frac{1}{M} \sum_{m=1}^M \frac{(Y[n_d, m] - Y_{ave})^4}{\rho^4} \tag{22}$$

where  $n_d$  is the number of range cells where the ACR target is located,  $\rho$  is the standard deviation of the spectral amplitude, and  $Y_{ave}$  is the average amplitude of the spectrum. Figure 8 shows time-sequential kurtosis extracted from the time-sequential spectrogram illustrated in Figure 6.

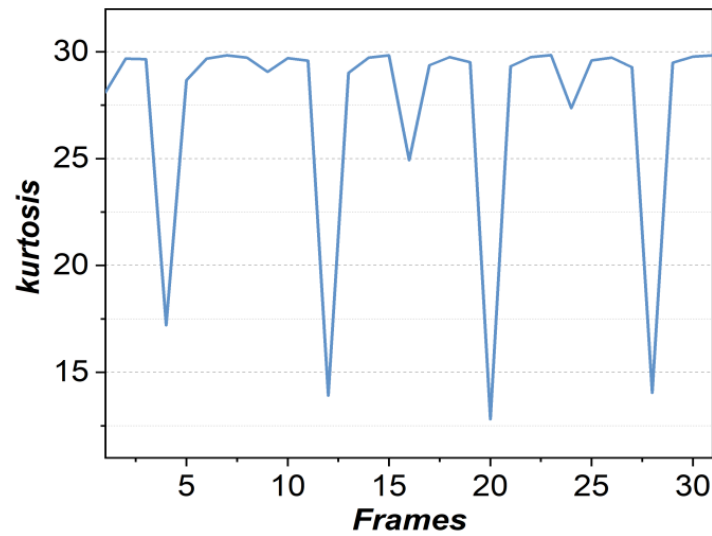


Figure 8. Time-sequential kurtosis diagram.

Kurtosis ( $K$ ) is a measure of fat tails for the probability density distribution of the spectrum. A higher  $K$  value, which represents a sharper Doppler spectrum shape, is more conducive to speed detection. In contrast, a lower  $K$  value means that the Doppler broadening is more severe. In Figure 8, the kurtosis ( $K$ ) varies with time-sequential frames. As one can see, the kurtosis is generally high in whole frames, while there is significant attenuation at a few moments, such as frames 4, 12, 20, and 28. The appearances of these kurtosis valleys exactly corresponds to the moments of Doppler broadening in Figure 6, which proves the rationality of employing kurtosis to measure the severity of Doppler broadening.

Furthermore, in order to quantitatively analyze the frequency of Doppler broadening, we determine whether the false dismissal occurs at frame  $t$  by

$$Q[t] = \begin{cases} 0 & \text{when } \max(Y[n_d, m]) > Thr \\ 1 & \text{when } \max(Y[n_d, m]) < Thr \end{cases} \quad (23)$$

where  $Q[t] = 1$  represents the occurrence of target false dismissal in the  $t$ -th frame,  $\max()$  is the operation of taking the maximum value from the data, and  $Thr$  is a fixed detection threshold. Figure 9 shows time-sequential judgements for the occurrence of false dismissal based on the time-sequential spectrogram illustrated in Figure 6.

It can be seen that there is a false dismissal of the target at frames 4, 12, 20, and 28, respectively, which exactly corresponds to the moments when the Doppler broadening occurs in Figure 6. By summing  $Q[m]$ , it can be concluded that the total times of false dismissal is four, which is consistent with the occurrence of Doppler broadening illustrated in Figure 6, proving the rationality of employing the number of false dismissals to measure the frequency of Doppler broadening.

Further analysis was conducted on the effects of different target conditions on the Doppler broadening phenomenon. Ten different values were selected for each of the five types of ACR target condition parameters: size, rotational rate, dropping velocity, height, and range. All values followed a linear increasing trend, as outlined in Table 1.

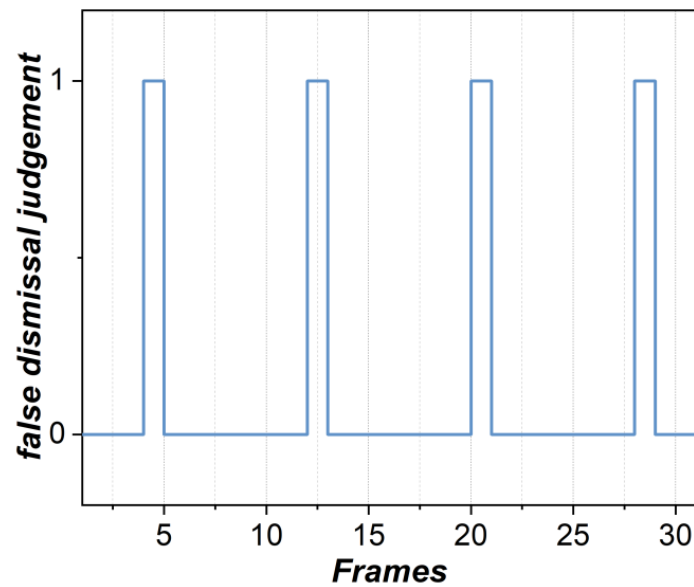


Figure 9. Time-sequential false dismissal judgement diagram.

Table 1. Selected values of ACR condition parameters.

No.	Size (m)	Rotation Rate (rad/s)	Dropping Velocity (m/s)	Height (m)	Range (m)
1	0.2	0.1	0.2	20	200
2	0.4	0.2	0.4	40	400
3	0.6	0.3	0.6	60	600
4	0.8	0.4	0.8	80	800
5	1.0	0.5	1.0	100	1000
6	1.2	0.6	1.2	120	1200
7	1.4	0.7	1.4	140	1400
8	1.6	0.8	1.6	160	1600
9	1.8	0.9	1.8	180	1800
10	2.0	1.0	2.0	200	2000

Continuing to adopt the simulation parameter settings mentioned in Figure 4, a therein single parameter would be transformed in turn by one value selected from Table 1 for each experiment. A total of 50 experiments were conducted to obtain 50 sets of time-sequential Doppler spectra. Then,  $K[m]$  and  $Q[m]$  were obtained from the 50 Doppler spectra. Finally, we collected the minimum kurtosis,  $\min(K[m])$ , and the false dismissal frequency,  $\text{sum}(Q[m])$ , representing the severity and frequency of the Doppler broadening phenomenon separately, as shown in Figure 10.

As one can see in Figure 10a, the severity of Doppler broadening is mainly related to the rotational rate of ACR. As the rotational rate gradually increases, the minimum kurtosis decreases, indicating that the degree of Doppler broadening becomes more severe. When the other four parameters change, the minimum kurtosis is almost constant, indicating that these parameters have little impact on the severity of the Doppler broadening phenomenon.

In Figure 10b, it can be seen that the frequency of Doppler broadening is also mainly related to the rotational rate of the ACR. As the rotational rate gradually increases, the number of false dismissals increases, indicating that the appearance of Doppler broadening becomes more frequent. When the other four parameters change, the number of false dismissals remains stable at around four, indicating that these parameters have little impact on the frequency of the Doppler broadening phenomenon.

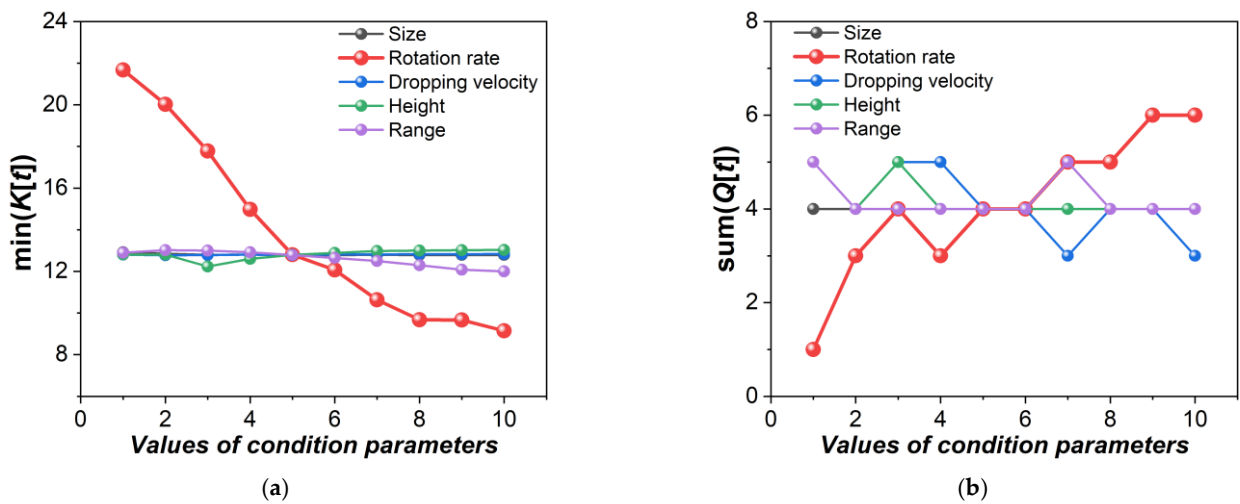


**Figure 10.** Doppler broadening phenomenon under different parameter schemes. (a) Doppler broadening severity for different parameter values. (b) Doppler broadening frequency for different parameter values.

Based on the above analysis, it can be concluded that the Doppler broadening phenomenon is likely related to the rotational motion of the ACR. The faster the ACR rotates, the more severe and more frequent the Doppler broadening phenomenon appears. Therefore, in order to avoid missed detections and achieve stable tracking of ACR targets, the design of ACRs should try to suppress their rotational motion trend as far as possible.

#### 4. Analysis of The Doppler Broadening Phenomenon Based on Rectangular Window Decomposition

To analyze the cause of the Doppler broadening phenomenon, the slow-time series and its spectrum at a particular moment of Doppler broadening were extracted as shown in Figure 11.

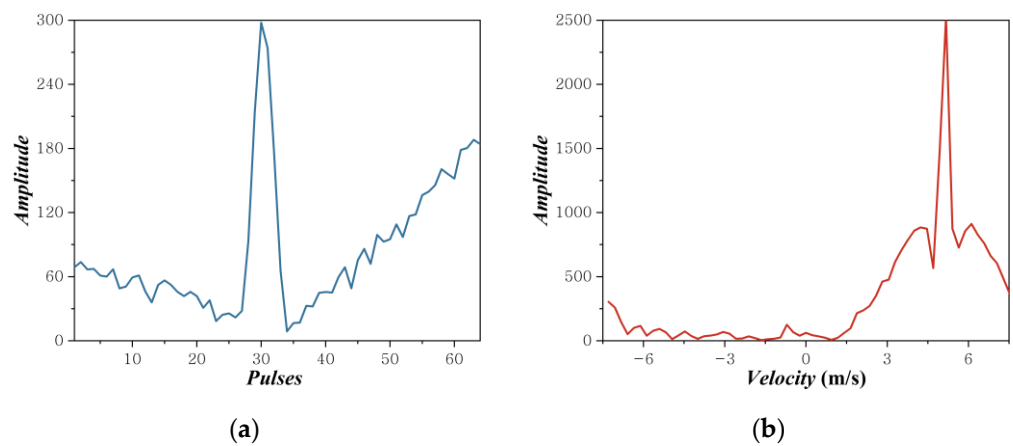


**Figure 11.** Broadening spectrum and its original slow-time series. (a) Amplitude fluctuation in the original slow-time series. (b) Doppler spectrum with broadening phenomena.

In Figure 11a, the horizontal coordinates represent pulse numbers, while the vertical coordinates depict the slow-time series amplitudes. In Figure 11b, the horizontal coordinates represent velocities, and the vertical coordinates represent spectral amplitudes. According to Figure 11, the Doppler spectrum at this moment exhibits significant broadening, while the corresponding original slow-time series demonstrates noticeable changes in amplitude oscillation. Conventional targets such as aircraft or ships typically maintain a constant echo amplitude (backscattered energy stabilization) within a CPI due to their stable navigational

attitude. Consequently, the target’s velocity information can be extracted by analyzing the phase change information of the slow-time series through DFT. However, the ACR target remains in a spin state for a prolonged period during airborne flight following launch, owing to its rotational rate. This results in a constant change in echo amplitude with attitude angle. Moreover, the slow-time series amplitude fluctuation of the ACR target is highly complex due to the uneven distribution of backscattered energy across the ACR’s angular domain. The amplitude fluctuation in the slow-time series generated by the ACR’s spin can be viewed as applying a specialized window function to the slow-time series. The form of this window function is intricate, and there is no universal expression for arbitrary conditions. Therefore, it necessitates case-by-case analysis.

As depicted in Figure 12, the slow-time series is simplified to the sum of four rectangular window functions for ease of analysis, with the following expressions:

$$\begin{aligned}
 A[m] &= A_1[m] + A_2[m] + A_3[m] + A_4[m] \quad (m = 0, \dots, M - 1) \\
 A_1[m] &= \begin{cases} a_1 & m = 0, \dots, M_1 - 1 \\ 0 & \text{else} \end{cases} \\
 A_2[m] &= \begin{cases} a_2 & m = M_1, \dots, M_2 - 1 \\ 0 & \text{else} \end{cases} \\
 A_3[m] &= \begin{cases} a_3 & m = M_2, \dots, M_3 - 1 \\ 0 & \text{else} \end{cases} \\
 A_4[m] &= \begin{cases} a_4 & m = M_3, \dots, M - 1 \\ 0 & \text{else} \end{cases}
 \end{aligned} \tag{24}$$

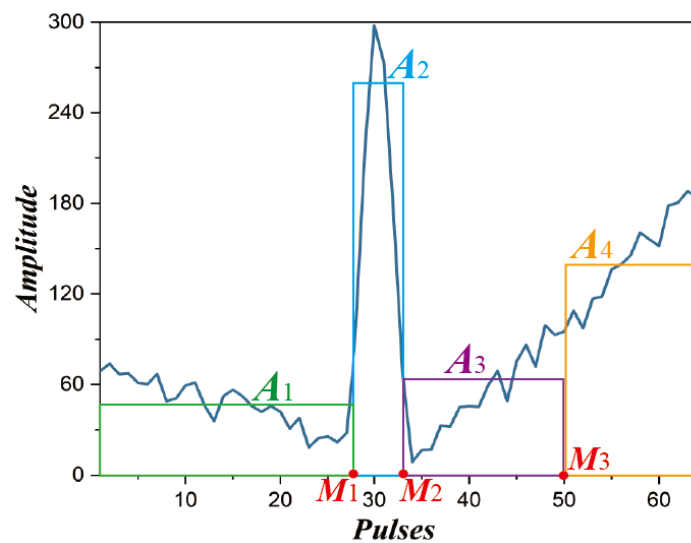


Figure 12. Simplified rectangular window for slow-time series amplitude.

By substituting the above equations into Equation (20), the slow-time series is

$$\begin{aligned}
 \chi'[m] &= \chi'_1[m] + \chi'_2[m] + \chi'_3[m] + \chi'_4[m] \\
 &= A_1[m] \exp(j2\pi f_d m T_r) + A_2[m] \exp(j2\pi f_d m T_r) \\
 &\quad + A_3[m] \exp(j2\pi f_d m T_r) + A_4[m] \exp(j2\pi f_d m T_r) \\
 &\quad (m = 0, \dots, M - 1)
 \end{aligned} \tag{25}$$

The following can be obtained according to the linear nature of the Fourier transform:

$$\begin{aligned}
 Y(f) &= \text{DTFT}(\chi'_1[m] + \chi'_2[m] + \chi'_3[m] + \chi'_4[m]) \\
 &= Y_1(f) + Y_2(f) + Y_3(f) + Y_4(f) \\
 &= a_1 \frac{\sin[\pi(f-f_d)M_1T_r]}{\sin[\pi(f-f_d)T_r]} \exp[-j\pi(M_1 - 1)(f - f_d)T_r] \\
 &\quad + a_2 \frac{\sin[\pi(f-f_d)(M_2-M_1)T_r]}{\sin[\pi(f-f_d)T_r]} \exp[-j\pi(M_1 + M_2 - 1)(f - f_d)T_r] \\
 &\quad + a_3 \frac{\sin[\pi(f-f_d)(M_3-M_2)T_r]}{\sin[\pi(f-f_d)T_r]} \exp[-j\pi(M_2 + M_3 - 1)(f - f_d)T_r] \\
 &\quad + a_4 \frac{\sin[\pi(f-f_d)(M-M_3)T_r]}{\sin[\pi(f-f_d)T_r]} \exp[-j\pi(M + M_3 - 1)(f - f_d)T_r] \\
 &\quad \left( -\frac{\text{PRF}}{2} \leq f < \frac{\text{PRF}}{2} \right)
 \end{aligned} \tag{26}$$

The Doppler spectrum of the simplified rectangular window slow-time series  $\chi'[m]$  can be obtained from the above equation, as illustrated in Figure 13.

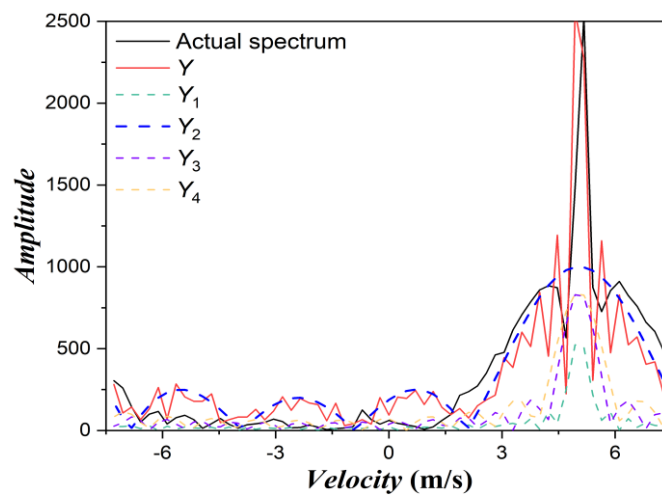


Figure 13. Doppler spectrum of slow-time series with rectangular window.

The variation in the total rectangular window slow-time series spectrum ( $Y$ ) in Figure 13 closely resembles that of the actual spectrum in Figure 11b. The broadening phenomenon observed in the ACR Doppler spectrum is precisely caused by the variation in the echo amplitude resulting from its spin. Analysis of the spectra of the slow-time series using four sub-rectangular window functions ( $Y_1, Y_2, Y_3,$  and  $Y_4$ ) indicates that the broadening of the spectra is primarily related to the rectangular window  $A_2$ . The higher amplitude of the rectangular window ( $A_2$ ) and its narrower width accentuate the flat trend of the asinc function in the spectrum.

To enhance generalization, the arbitrary slow-time series amplitude is expressed as the sum of  $M/2q$  rectangular window functions with the following expressions:

$$\begin{aligned}
 A[m] &= \sum_{i=0}^{\frac{M}{2q}-1} A_i[m] \quad (m = 0, \dots, M - 1) \\
 A_i[m] &= \begin{cases} |\chi[2qi]| & m = 2qi, \dots, 2qi + 2q \\ 0 & \text{else} \end{cases}
 \end{aligned} \tag{27}$$

Then, the slow-time series can be re-expressed as

$$\begin{aligned}
 \chi'[m] &= \sum_{i=0}^{\frac{M}{2q}-1} A_i[m] \exp(j2\pi f_d m T_r) \\
 &\quad (m = 0, \dots, M - 1)
 \end{aligned} \tag{28}$$

DTFT on the new slow-time series  $\chi'[m]$  yields

$$\begin{aligned}
 Y(f) &= \text{DTFT} \left( \sum_{i=0}^{\frac{M}{2q}-1} A_i[m] \exp(j2\pi f_d m T_r) \right) \\
 &= \sum_{i=0}^{\frac{M}{2q}-1} |\chi[2qi]| \frac{\sin[\pi(f-f_d)2qT_r]}{\sin[\pi(f-f_d)T_r]} \exp[-j\pi(4qi + 2q - 1)(f - f_d)T_r] \quad (29) \\
 &= \frac{\sin[\pi(f-f_d)2qT_r]}{\sin[\pi(f-f_d)T_r]} \sum_{i=0}^{\frac{M}{2q}-1} |\chi[2qi]| \exp[-j\pi(4qi + 2q - 1)(f - f_d)T_r] \\
 &\quad \left( -\frac{PRF}{2} \leq f < \frac{PRF}{2} \right)
 \end{aligned}$$

The spectrum function has the following characteristics:

1. When  $f = f_d$ , the phase of the spectra generated by all rectangular window slow-time series is 0. In this case, the total spectral amplitude equals the sum of all sub-spectral amplitudes. However, when  $f \neq f_d$ , the spectra of all rectangular window slow-time series do not interact with each other. Consequently, the amplitude will decay significantly. Therefore, the spectrum always peaks at  $f = f_d$  regardless of the value of  $q$ ;
2. By changing the value of  $q$ , different fitting effects can be achieved. A larger  $q$  value results in fewer required rectangular windows and a simpler shape of the spectrum. Conversely, a smaller  $q$  value results in more required rectangular windows and a more complex shape of the spectrum;
3. A small  $q$  value results in flatter asinc functions. When the amplitude of a specific rectangular window,  $A_x$ , is significantly higher than the other rectangular windows, the interference effect of the other rectangular windows on the spectrum of  $A_x$  is reduced. This leads to an apparent broadening phenomenon in the total spectrum. Additionally, if there are multiple rectangular windows with prominent amplitudes and small phase differences between their spectra, the total spectrum will also broaden.

Based on the above analysis, the Doppler broadening of ACRs is caused by the unique variation in amplitude in the slow-time series. When the amplitude of a consecutive set of pulses ( $M_h$ ) in the slow-time series is significantly higher than the others, it leads to Doppler spectral broadening. This broadening phenomenon becomes more noticeable with smaller values of  $M_h$ . The variation in amplitude in the slow-time series is determined by the echo amplitude ( $A_r$ ), which is, in turn, determined by the RCS value of the ACR.

The RCS variation of an ACR with the aspect angle [11] is depicted in Figure 14. The rotational motion of the ACR induces continuous changes in the relative incidence angle of the radar beam, consequently leading to fluctuations in its RCS. As shown in Figure 14, there will be a sharp increase or decrease in ACR backscattered energy near certain angles. The Doppler broadening phenomenon exhibited by the ACR arises precisely due to the fact that the aspect angle aligns with these critical angles within a coherent processing interval (CPI), resulting in a few pulse repetition intervals (PRIs) collecting higher amplitudes and forming distinctive amplitude variations in a slow-time series.

In conclusion, the rotational motion of an ACR leads to a sharp change in its RCS amplitude at certain moments, which is reflected as broadening in the spectrum. This explains why the severity and frequency of Doppler broadening are related to the rotational rate and proves the correctness of the analysis results in Section 3.

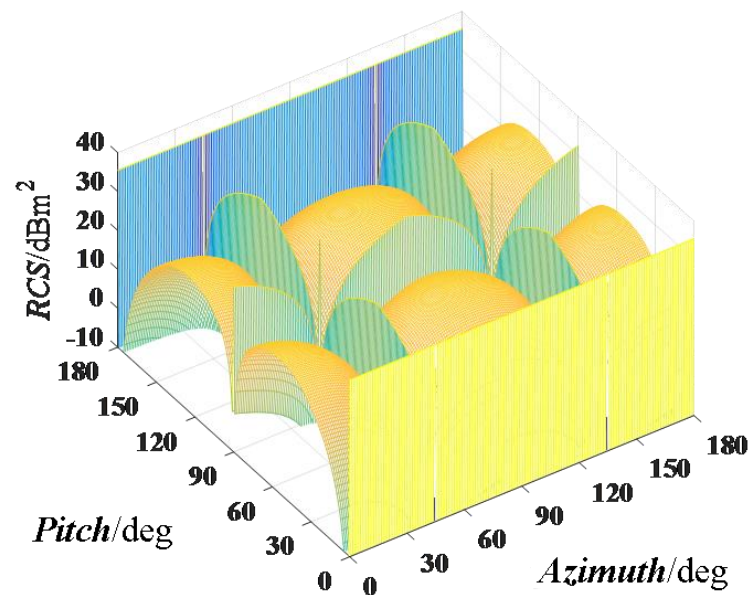


Figure 14. Omnidirectional RCS of ACR.

## 5. Conclusions

Based on the constructed ACR radar echo signal model, the dynamic Doppler characteristics are investigated through pulse Doppler processing. The effects of various ACR condition parameters on the severity and frequency of Doppler broadening are analyzed. Finally, a simplified rectangular window method is proposed for in-depth analysis, which helps to identify the intrinsic causes of the Doppler broadening phenomenon. The detailed analysis of the dynamic Doppler characteristics of ACRs enhances the understanding of their working mechanisms, laying a theoretical foundation for future in-depth research on the application, detection, and identification of this type of equipment.

This research was conducted during the steady dropping phase of an ACR. Analyzing the Doppler characteristics of ACRs in the initial stage after launch poses greater challenges, which will be the focus of our future endeavors.

**Author Contributions:** Conceptualization, L.W.; methodology, L.W. and S.H.; software, L.W. and S.H.; validation, Z.L.; formal analysis, L.W. and Y.L.; investigation, L.L. and Y.L.; resources, L.W. and C.F.; data curation, L.W.; writing—original draft preparation, L.W.; writing—review and editing, L.W.; visualization, L.W.; supervision, C.F.; project administration, S.H.; funding acquisition, S.H. All authors have read and agreed to the published version of the manuscript.

**Funding:** This research received no external funding.

**Institutional Review Board Statement:** Not applicable.

**Informed Consent Statement:** Not applicable.

**Data Availability Statement:** The data that support the findings of this study are available within the article.

**Conflicts of Interest:** The authors declare no conflicts of interest.

## References

- Cardillo, E.; Ferro, L. Multi-Frequency Analysis of Microwave and Millimeter-Wave Radars for Ship Collision Avoidance. In Proceedings of the Microwave Mediterranean Symposium (MMS), Pizzo Calabro, Italy, 9–13 May 2022. [[CrossRef](#)]
- Hu, H.; Zhang, L.; Zhang, X. A study on equipment developments and operational using of ship born gas-filled anti-missile multi-corner reflector. *Def. Technol. Rev.* **2018**, *39*, 74–77.
- Gan, L.; Sun, G.; Feng, D.; Li, J. Characteristics of an Eight-Quadrant Corner Reflector Involving a Reconfigurable Active Metasurface. *Sensors* **2022**, *22*, 4715. [[CrossRef](#)]

4. Kubicke, G.; Bourlier, C.; Saillard, J. Comparison of bistatic signatures of octahedral and icosahedral reflectors in high-frequency domain. In Proceedings of the European Microwave Conference, Munich, Germany, 9–12 October 2007.
5. Kubicke, G.; Bourlier, C.; Saillard, J. Polarimetric bistatic signature of a faceted octahedron in high-frequency domain. *Prog. Electromagn. Res.* **2007**, *71*, 173–209. [[CrossRef](#)]
6. Kubicke, G.; Bourlier, C.; Saillard, J. High-Frequency Bistatic Scattering by Depolarizing, Nearly Omnidirectional Reflectors: Higher Order Polyhedral Reflectors. *IEEE Trans. Antennas Propag.* **2008**, *56*, 3029–3035. [[CrossRef](#)]
7. Zhang, J.; Hu, S.; Wang, P.; Xueman, F. RCS model construction and analysis for corner reflector based on PO/AP algorithm. *Syst. Eng. Electron.* **2018**, *40*, 1478–1485.
8. Cong, Z.; He, Z.; Taiping, S.; Ding, D.; Chen, R. A local current based iterative physical optics method for computing the RCS of target above sea surface. *Eng. Anal. Bound. Elem.* **2023**, *146*, 318–326. [[CrossRef](#)]
9. Luo, Y.; Guo, L.; Zuo, Y. Investigations of Effects of Geometric Characteristics on RCS for Corner Reflectors. In Proceedings of the International Conference on Computational Electromagnetics, Shanghai, China, 20–22 March 2019.
10. Wu, L.; Hu, S.; Xu, J.; Liu, Z. Dynamic sequential radar cross section properties of airborne corner reflector in array. *IET Radar Sonar Navig.* **2023**, *17*, 1405–1419. [[CrossRef](#)]
11. Wu, L.; Hu, S.; Zhang, J.; Weng, Y.; Li, S.; Yang, J.; Yi, H. Fast RCS Estimation Method for Bipyramid Corner Reflector. *Tactical Missile Technol.* **2021**, *5*, 29–35.
12. Bai, J.; Qin, P.; Li, H.; Zhang, R.; Zhang, X. An Improved Adaptive Pulse Compression Algorithm Based on Linear Frequency Modulation Signal. In Proceedings of the IEEE International Conference on Signal, Information and Data Processing (ICSIDP), Chongqing, China, 11–13 December 2019. [[CrossRef](#)]
13. Wu, L.; Xu, J.; Hu, S.; Liu, Z. High-frequency backscattering properties of quasi-omnidirectional corner reflector: The great-icosahedral-like reflector. *AIP Adv.* **2022**, *12*, 105225. [[CrossRef](#)]
14. Ding, L.; Geng, F.; Chen, J. *Radar Principles*, 6th ed.; Publishing House of Electronics Industry: Beijing, China, 2020; pp. 47–65.
15. Richards, M.A. *Fundamentals of Radar Signal Processing*, 2nd ed.; McGraw-Hill Education: New York, NY, USA, 2005; pp. 34–45.
16. Fan, X.; Hu, S.; He, J. High-frequency method for the evaluation of the radar cross section of corner reflectors. *Chin. J. Radio Sci.* **2016**, *31*, 331–335+362.
17. Bjorklund, S.; Nelander, A.; Pettersson, M.I. Fast-Time and Slow-Time Space-Time Adaptive Processing for bistatic radar interference suppression. In Proceedings of the IEEE National Radar Conference, Arlington, VA, USA, 10–15 May 2015.
18. Mahafza, B.R. *Radar Systems Analysis and Design Using MATLAB*, 3rd ed.; CRC Press: Boca Raton, FL, USA, 2016; pp. 316–330.
19. Dwivedi, Y.; Rao, S.S. A test for second order stationarity of a time series based on the Discrete Fourier Transform (Technical Report). *J. Time* **2015**, *32*, 68–91. [[CrossRef](#)]
20. Alabaster, C. *Pulse Doppler Processing*; IET Digital Library: London, UK, 2012; pp. 35–61.
21. Zhang, J.; Cheng, G.; Tang, J.; Wu, H.; Tian, Z. A Subaperture Motion Compensation Algorithm for Wide-Beam, Multiple-Receiver SAS Systems. *J. Mar. Sci. Eng.* **2023**, *11*, 1627. [[CrossRef](#)]
22. Ermoshkin, A.V.; Kosteev, D.A.; Ponomarenko, A.A.; Razumov, D.D.; Salin, M.B. Surface Waves Prediction Based on Long-Range Acoustic Backscattering in a Mid-Frequency Range. *J. Mar. Sci. Eng.* **2022**, *10*, 722. [[CrossRef](#)]
23. Yang, Y.; Fang, S. Improved Velocity Estimation Method for Doppler Sonar Based on Accuracy Evaluation and Selection. *J. Mar. Sci. Eng.* **2021**, *9*, 576. [[CrossRef](#)]
24. Skrai, K.; Petrovi, J.; Pale, P. Classification of Low- and High-Entropy File Fragments Using Randomness Measures and Discrete Fourier Transform Coefficients. *Vietnam J. Comput. Sci.* **2023**, *10*, 433–462. [[CrossRef](#)]
25. Li, P.; Wu, Y.; Guo, W.; Cao, C.; Ma, Y.; Li, L.; Leng, H.; Zhou, A.; Song, J. Striation-Based Beamforming with Two-Dimensional Filtering for Suppressing Tonal Interference. *J. Mar. Sci. Eng.* **2023**, *11*, 2117. [[CrossRef](#)]
26. Varbanets, R.; Fomin, O.; Píšťek, V.; Klymenko, V.; Minchev, D.; Khrulev, A.; Zalozh, V.; Kučera, P. Acoustic Method for Estimation of Marine Low-Speed Engine Turbocharger Parameters. *J. Mar. Sci. Eng.* **2021**, *9*, 321. [[CrossRef](#)]
27. Liu, S.; Guo, H.; Qian, Z.; Li, J.; Wang, X.; Sun, W.; Zhang, L.; Zhang, A. A Study on a Novel Inverted Ultra-Short Baseline Positioning System and Phase Difference Estimation. *J. Mar. Sci. Eng.* **2023**, *11*, 952. [[CrossRef](#)]
28. Ye, R.; Xing, H.; Zhou, X. Sea-Surface Small Target Detection Based on Improved Markov Transition Fields. *J. Mar. Sci. Eng.* **2024**, *12*, 582. [[CrossRef](#)]
29. Zhang, F.; Zhang, W.; Cheng, C.; Hou, X.; Cao, C. Detection of Small Objects in Side-Scan Sonar Images Using an Enhanced YOLOv7-Based Approach. *J. Mar. Sci. Eng.* **2023**, *11*, 2155. [[CrossRef](#)]
30. Zhao, D.; Xing, H.; Wang, H.; Zhang, H.; Liang, X.; Li, H. Sea-Surface Small Target Detection Based on Four Features Extracted by FAST Algorithm. *J. Mar. Sci. Eng.* **2023**, *11*, 339. [[CrossRef](#)]
31. Foss, T.; Joreskog, K.G.; Olsson, U.H. Testing structural equation models: The effect of kurtosis. *Comput. Stat. Data Anal.* **2011**, *55*, 2263–2275. [[CrossRef](#)]
32. Zhang, X.; Yang, P. Back Projection Algorithm for Multi-Receiver Synthetic Aperture Sonar Based on Two Interpolators. *J. Mar. Sci. Eng.* **2022**, *10*, 718. [[CrossRef](#)]

33. Flamarion, M.V.; Pelinovsky, E. Evolution and Statistical Analysis of Internal Random Wave Fields within the Benjamin–Ono Equation. *J. Mar. Sci. Eng.* **2023**, *11*, 1853. [[CrossRef](#)]
34. Dai, Z.; Li, H.; Wang, C.; He, Y. Backscattering Statistics of Labeled Sentinel-1 Wave Mode Imagettes for Ten Geophysical Phenomena. *J. Mar. Sci. Eng.* **2022**, *10*, 1594. [[CrossRef](#)]

**Disclaimer/Publisher’s Note:** The statements, opinions and data contained in all publications are solely those of the individual author(s) and contributor(s) and not of MDPI and/or the editor(s). MDPI and/or the editor(s) disclaim responsibility for any injury to people or property resulting from any ideas, methods, instructions or products referred to in the content.